Plume Study of an Electrospray Thruster Using a HAN-Based Dual-Mode Ionic Liquid Propellant

IEPC-2022-190

Presented at the 37th International Electric Propulsion Conference
Massachusetts Institute of Technology, Cambridge, MA, USA
June 19-23, 2022

Chengyu Ma[1], Vincenzo Messina[2], and Charles N. Ryan[3]
University of Southampton, Southampton, Hampshire, United Kingdom, SO17 1BJ

Joshua L. Rovey[4], Zachary Putnam[5], and Michael Lembeck[6]
University of Illinois Urbana-Champaign, Urbana, IL 61801, United States

Steven Berg[7]
Froberg Aerospace LLC., Wilmington, NC 28401, United States

This paper investigates the electrospray performance of FAM-110A, a novel hydroxylammonium nitrate (HAN) based ionic liquid propellant developed for a chemical-electric dual-mode space propulsion system. FAM-110A was tested using a PET-100 electrospray thruster with a porous emitter, and its electrospray performance was compared with the widely used 1-Ethyl-3-methylimidazolium tetrafluoroborate (EMI-BF_4) propellant. The FAM-110A thrusters demonstrated a lower onset voltage and comparably high emission current. An external electric field was applied in front of the plume collecting plate to study the current measurement accuracy and the effect of secondary species emissions from high-energy particles colliding on the surface. The spatial distribution of the thruster plume current was profiled using a 2-axis rotary stage. Both FAM-110A and EMI-BF_4 showed asymmetrical plume profiles, with FAM-110A having a smaller overall plume angle. The energy distribution of the plume particles was measured using a retarding potential analyzer, and the results showed that the FAM-110A had a highly mono-energetic plume with little evidence of fragmentation in the field-free region. Light emission in electrospray thruster operation was observed using long-exposure photography. This plume characterization study suggests that FAM-110A can be run in porous electrospray thrusters with promising performance, and further development of this technology is recommended.

I. Introduction

Electrospray propulsion is an electrostatic propulsion concept with promising applications on nanosatellites [1]. An electrospray thruster generally uses an ionic liquid with low vapor pressure as the propellant. The liquid is held on an emitter, usually in the shape of a capillary or a sharp spike/tip. An extractor electrode with apertures is placed near the emitter. A high voltage is applied between the emitter and the extractor to electrostatically extract charged particles from the liquid fed to the emitter tips, thus, generating thrust. Over the last decade of study and development, the propulsive performance of electrospray thrusters has been improved significantly. A unique feature of electrospray thrusters is that they can maintain relatively high efficiency when operated at low power, suitable for nanosatellite

[1]Research Fellow, Department of Aeronautics and Astronautics, Southampton, Hampshire, SO17 1BJ, United Kingdom.
[2]Graduate Research Assistant, Department of Aeronautics and Astronautics, Southampton, Hampshire, SO17 1BJ, United Kingdom.
[3]Lecturer/Assistant Professor, Department of Aeronautics and Astronautics, Southampton, Hampshire, SO17 1BJ, United Kingdom.
[4]Associate Professor, Aerospace Engineering, Talbot Laboratory 104 S Wright St, Urbana, IL 61801, United States.
[5]Assistant Professor, Aerospace Engineering, Talbot Laboratory 104 S Wright St, Urbana, IL 61801, United States.
[6]Clinical Associate Professor, Aerospace Engineering, Talbot Laboratory 104 S Wright St, Urbana, IL 61801, United States.
[7]Assistant Professor, Chief Executive Office, Froberg Aerospace LLC, 226 N. Front St. Ste. 123, Wilmington, NC 28401, United States.

applications. With the use of new ionic liquids, such as 1-Ethyl-3-methylimidazolium tetrafluoroborate (EMI-BF_4) and 1-Ethyl-3-methylimidazolium bis(trifluoromethylsulfonyl)imide (EMI-Im), electrospray thrusters can emit molecular ions with little to no droplet, and delivery a high specific impulse of 1000 to 4000 s [1–6]. However, the low thrust is a challenging aspect of electrospray thrusters, currently usually found to be below 100 μN. This thrust level limits electrospray thruster applications to mostly nanosatellite-class missions with slow acceleration.

In order to expand the applicable missions using electrospray propulsion, a dual-mode propulsion system was proposed by the University of Illinois Urbana-Champaign [7, 8]. The system consists of a mono-propellant chemical thruster that delivers high thrust and an electrospray thruster that delivers high specific impulse, with both thrusters using the same HAN-based propellant, FAM-110A [8, 9]. The concept is illustrated in Figure 1. FAM-110A is an ionic liquid mixture of 59% of hydroxylammonium nitrate (HAN) and 41% of Ethyl-3-methylimidazolium ethyl-sulfate (EMIM-$EtSO_4$) [10]. As the same propellant is used in both the electric and chemical modes, it can use more compact propellant storage and delivery system compared to a fully separate chemical and electric hybrid mode propulsion system [11]. With the flexibility of changing thrust and specific impulse and sharing of one propellant storage, this dual-mode propulsion system has potential to support a versatile variety of spacecraft missions with complicated requirements, including in-orbit servicing, capturing and de-orbiting, refueling, and debris avoiding [7, 12].

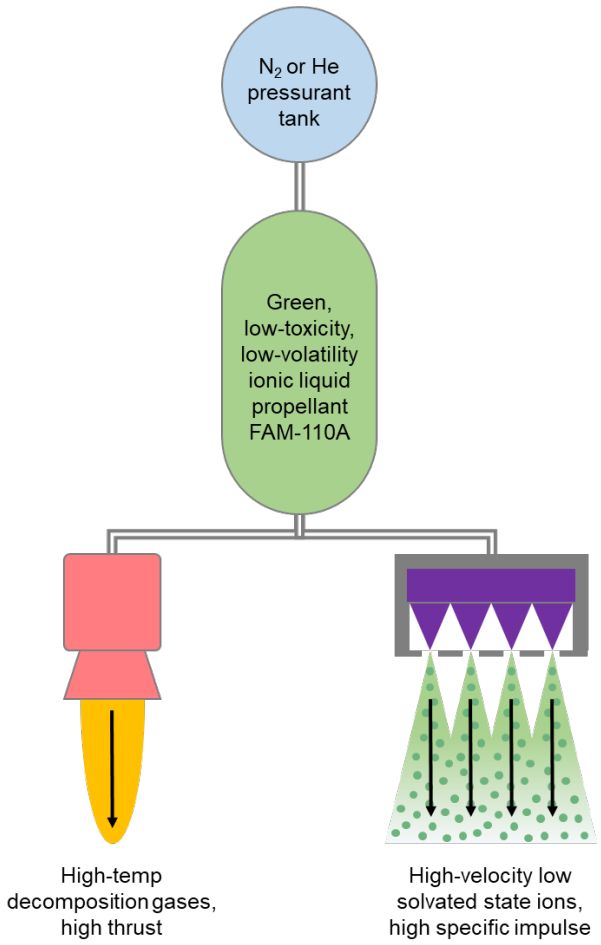

Fig. 1 An illustration of the decomposition-electrospray dual-mode propulsion system concept using FAM-110A propellant [7].

The performance of FAM-110A in a chemical thruster has been reported in a recently presented paper [13]. Regarding the electric mode, FAM-110A has been tested in capillary-emitter electrospray thrusters, which confirmed its feasibility as an electrospray propellant [8, 10]. However, the compatibility of FAM-110A is yet untested in a porous-emitter electrospray thruster, currently the most typically developed electrospray thruster. This research investigates the FAM-110A electrospray performance using the PET-100 electrospray thruster with a porous emitter developed at the

University of Southampton. This project is a collaboration between the University of Illinois Urbana-Champaign and the University of Southampton, and it was funded by DARPA with the objective of investigating the propulsion performance using FAM-110A in a monopropellant decomposition thruster and a porous-emitter electrospray thruster.

II. Propellant Synthesis and Compatibility Study

The FAM-110A propellant used in this study was synthesized in the David Fearn Electric Propulsion Laboratory at the University of Southampton, with the newly built synthesis station shown in 2. Following the method developed by the University of Illinois, Urbana-Champaign, the synthesis process consists of three parts: purifying the EMIM-$EtSO_4$ solution, drying the HAN solution, and mixing the two reagents to form the FAM-110A solution. The EMIM-$EtSO_4$ was sourced from IoLiTec-Ionic Liquids Technologies GmbH in a 98% aqueous solution, and HAN was purchased from SelectLab Chemicals GmbH in a 20% aqueous solution. Both EMIM-$EtSO_4$ and HAN were dried using an IKA RV 3 V rotary evaporator, with the vertical condensing glassware connected to a vacuum of 10^{-2} mbar. With the rotary speed set to 60 rpm and the water bath temperature set to 50°C, the EMIM-$EtSO_4$ was dried in the rotary flask for 6 hours for a sufficient amount of water to evaporate, then, the concentrated EMIM-$EtSO_4$ of >99% was stored in a sealed glass container. The first step of HAN drying process was the same, but as HAN is highly hygroscopic, the water evaporation rate significantly decreases as the HAN concentration exceeds roughly 90%. Hence, an additional step of azeotropic distillation was adapted, which further enhances the water evaporation by adding IPA into the mixture until the water is <12% by mass. This HAN-H_2O-IPA mixture was put in a vacuum for 12 hours, allowing the water and IPA to evaporate and leaving crystallized HAN in the flask with a concentration >99%. The vacuum pressure was carefully controlled to avoid vigorous boiling of IPA and water. Note that for the crystallization to occur, the raw HAN solution from the supplier needs to be of high purity. In this study, the HAN supplied from SelectLab Chemicals GmbH was fabricated in 99% purity below diluted in a 20% aqueous solution, which repeatedly yield HAN crystallization. Noteworthy, in an earlier attempt, HAN purchased from the same supplier at 98% purity in 20% aqueous solution did not form crystals after the same drying procedures. Finally, the FAM-110A propellant is synthesized by mixing the dried HAN crystals with the dried EMIM-$EtSO_4$ following the mass ratio of 41:59. Note that due to FAM-110A's inherent tendency of unstable decomposition, only a small amount of FAM-110A, roughly 10 to 15 ml, was prepared before each test campaign, and the remaining FAM-110A solution was diluted to 10% aqueous solution immediately after each test.

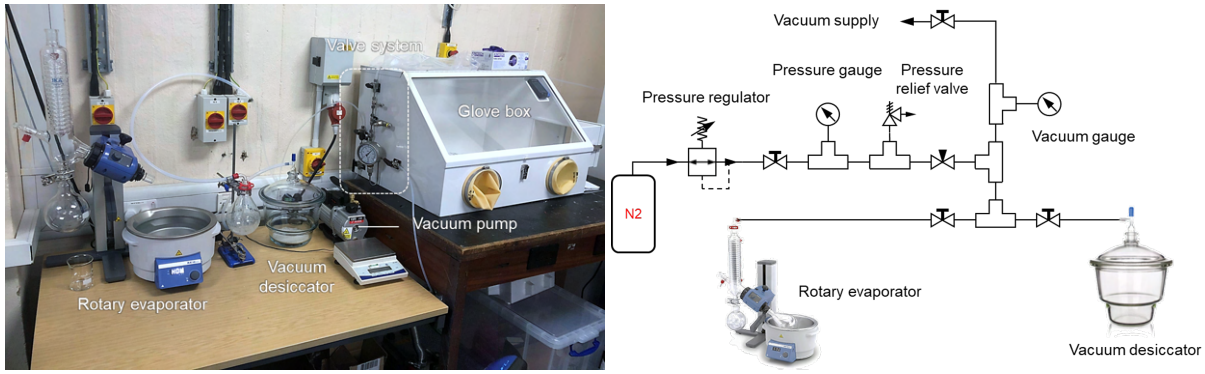

(a) Synthesis station.

(b) Pressure control system.

Fig. 2 FAM-110A propellant synthesize station.

The HAN composition in the FAM-110A propellant is reactive with a wide range of materials, and thus, a material compatibility study was conducted to select suitable materials for thruster design. In total, six materials were tested: porous borosilicate glass (P3 and P0 grades), mild steel, 304 stainless steel, 316 stainless steel, 5083 aluminum alloy, and molybdenum. Note that the borosilicate glass, 304 and 316 stainless steel are porous blocks, and their large internal surface areas could enhance the rate of chemical reaction with FAM-110A, if any. These materials were put in separate borosilicate glass beakers, and each filled 3 mm deep with the FAM-110A ionic liquid. The beakers were placed in a vacuum desiccator for two months, and then the materials and the ionic liquid in each beaker were inspected. The results are shown in 3. The ionic liquid mixture with the porous 304 stainless steel part started to bubble in a vacuum within one hour, suggesting chemical reactions between the liquid and the metal part. The porous 316 stainless steel

part seemed more stable than the 304 grade as it did not show acute bubbling on the first day; however, after two months, there was no more liquid in the beaker, and the part was dry, suggesting that the 316 stainless steel is still mildly reactive to the FAM-110A. The mild steel part was severely corroded, the structure was dissolved, and the color of the ionic liquid changed from clear to brown within the first week. The molybdenum parts also showed evidence of corrosion, with surface color changed to dark, and liquid color turned to yellow. The aluminum alloy part seemed more stable as only its surface turned white, and there was no noticeable change in the liquid. The porous borosilicate glass parts appeared to be inert to FAM-110A, as they did not show any evidence of change with the material and the liquid. It should be noted that previous studies on HAN compatibility suggest titanium is chemically inert to HAN, thus suitable to work as electrical contacts [14–16]. However, titanium was not investigated in this study.

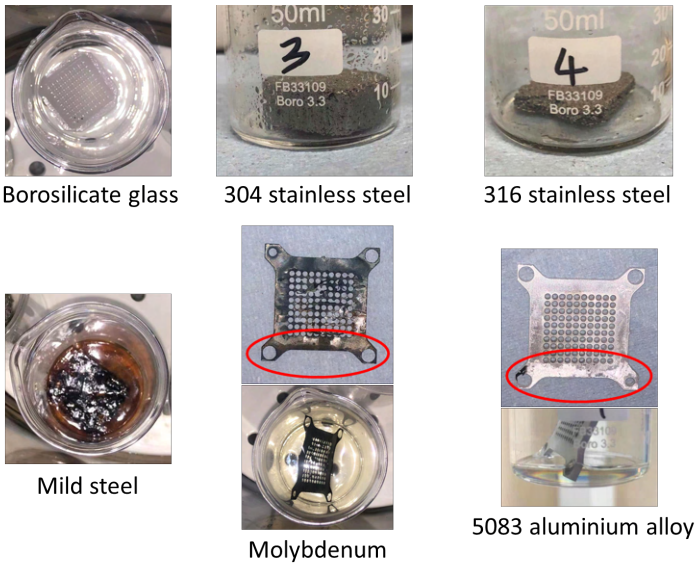

Fig. 3 Materials after two months of compatibility test with FAM-110A ionic liquid.

III. Thruster Design and Test Apparatus

The thruster used in this study was slightly modified from the PET-100 electrospray thruster designed at the University of Southampton [6, 17]. It consists of a porous emitter with 100 emission tips, which were made of CNC machined P4 grade and P5 grade borosilicate glass. A reservoir made of P0 grade borosilicate glass was placed underneath the emitter. The emitter and the reservoir were enclosed in a set of plastic cases. Three sets of cases were manufactured, including a 3D-printed resin casing, a CNC machined Acrylic case, and a CNC machined polyetheretherketone (PEEK) case. Due to project schedule reasons, the extractor electrode was made of mild steel, which will be replaced by titanium in future studies. The extractor was placed on top of the casing, and the extractor apertures were made using waterjet cutting. Note that the extractor was made of mild steel instead of the better-suited material titanium due to the issues with the project schedule. A 316 stainless steel 1/16 inch Swagelok Union connector was placed at the backside of the thruster and in contact with the reservoir to conduct power to the emitter. The Swagelok connector was also used as a fluidic connector as a part of a pressurized propellant feeding system [18]. This paper focuses on the thruster study of the FAM-110A and EMI-BF_4 with a passive propellant feeding method, which utilizes capillary actions between the finer-porosity emitter and the coarser-porosity reservoir. Note that in future thruster designs, all metal parts in contact with FAM-110A ionic liquid would be made of titanium due to its chemical inertness. Two identical thrusters were made, one tested using EMI-BF_4 propellant and the other tested using FAM-110A propellant. The thruster with EMI-BF_4 was used as a benchmark model in quantifying and comparing the performance of FAM-110A.

Before the tests, the emitters were scanned using an InfiniteFocus focus-variation profiler sourced from Alicona Imaging GmbH, and the results are shown in 5. The average values (ave) and standard deviations (std) regarding the height (h_t) and tip curvature radius (r_t) of the P5 and P4 grade emitters are listed in Table 1. In comparison, the P5 grade emitter had sharper tips, smoother surface and better uniformity in tip radius and height. The overall geometrical uniformity of these emitters was improved than previous manufacturing batches [6, 19], which is beneficial in terms of

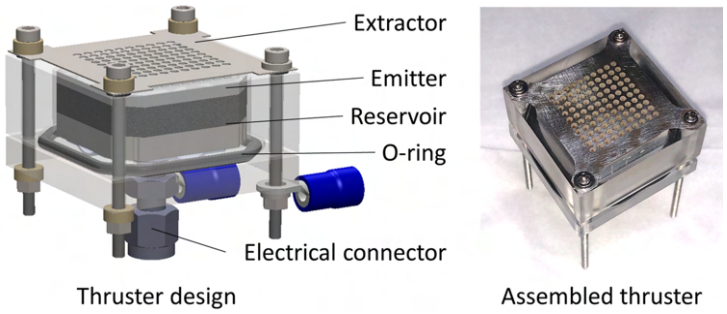

Fig. 4 PET-100 thruster designed for FAM-110A propellant.

Table 1 The mean (ave) and standard deviation (std) of the emission tip heights and apex curvature radii.

Porosity	h_t ave, mm	h_t std, μm	r_t ave, μm	r_t std, μm
P5	1.8829	7.534	45.095	7.439
P4	1.8059	45.93	77.533	10.963

emission stability.

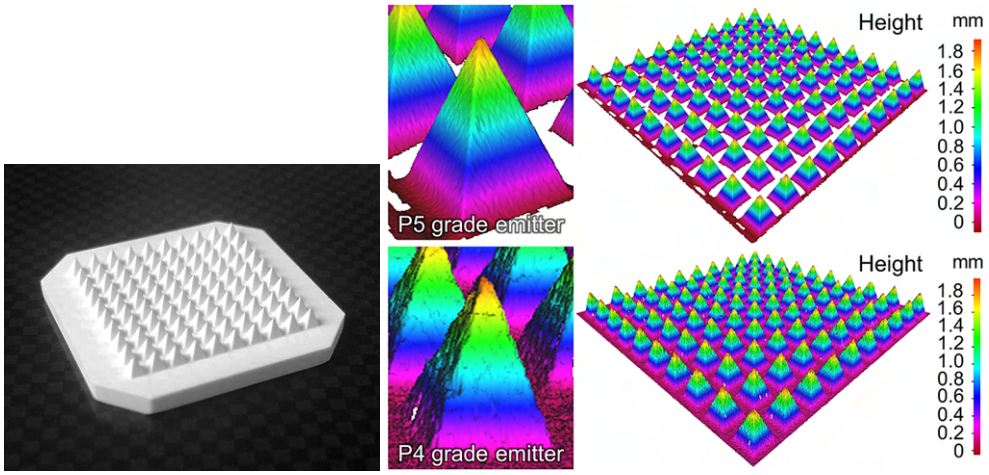

(a) A CNC machined P5 grade emitter. (b) 3D profile of a P5 grade emitter and a P4 grade emitter.

Fig. 5 3D profiles of CNC machined emitters.

The electrospray thrusters were tested in a vacuum system in David Fearn Electric Propulsion Laboratory at the University of Southampton. The smaller vacuum chamber is equipped with a turbopump and the vacuum level was kept between 10^{-5} to 10^{-6} mbar throughout the thruster testing. The overall test set up is shown in Figure 6. The investigated tests include current-voltage characterization, spatial plume profile measurement, retarding potential analysis, and long-exposure imaging of light emission phenomena from ion impingement on different materials.

The high voltage power supply used for the electrospray thruster was the AMT-5B20-L1 Ultra High-Speed High-Voltage Amplifier sourced from Matsusada Precision Inc., whose voltage output limit is ±5 kV with ±20 mA of current limit. An additional high voltage power supply, HCP 350-12500 sourced from FuG Elektronik GmbH, was used in RPA tests. For high-efficiency experimental characterization, the thruster was mounted on a 2-axis rotary stage, which can rotate the thruster and point it to different probes. A plume collector was placed in the plume to measure the current of intercepted particles. An RPA was used to measure the energy distribution of particles in the plume. An integrated DAQ and control system was built with a National Instrument system and a LabVIEW interface. The system can program and monitor power supply output, and it contains a set of load resistors, operational amplifiers and potential dividers that monitor current flow through the extractor, the collector, and the RPA probe.

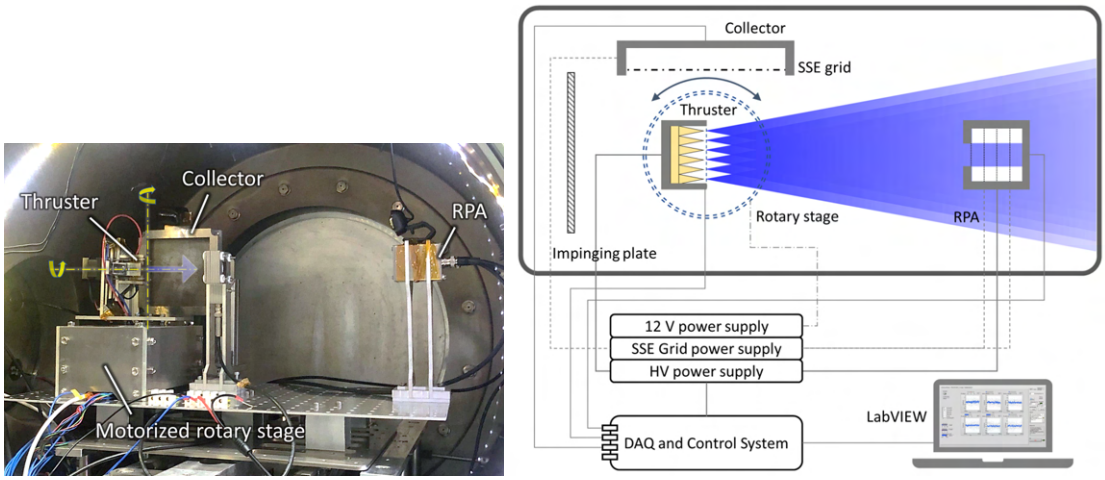

(a) Test setup.

(b) Electrical diagram.

Fig. 6 The electrospray test system in a vacuum chamber in the David Fearn Electric Propulsion Laboratory.

IV. Current-voltage Characteristics

The plume collector had a molybdenum plate to measure the current of the intercepted plume. In front of the molybdenum, a nickel mesh, MN17 from Precision Eforming LLC, was applied with a voltage to suppress the emission of secondary electrons from ions colliding with the plate. The collector was 15 × 15 cm in size, and placed approximately 15 cm away from the thruster extractor location.

The electrospray thruster operated in a bipolar mode where the extractor kept ground potential while the emitter potential was periodically switched between positive and negative polarities, with a frequency of 0.25 Hz. The current-voltage characteristics of the electrospray thrusters running using FAM-110A and EMI-BF_4 are shown in Figure 7. In the two tests, both thrusters used the same configuration, with a P5 grade emitter, a P0 grade reservoir, and the emitter tips aligned to the plane of the extractor upstream surface.

The FAM-110A thruster was tested from the onset voltage of ±1500 V up to ±2000 V. Within this range, the emission current appeared to be relatively stable, only with minor and high-frequency variations over time. The EMI-BF_4 thruster was tested from the onset voltage ±1900 V up to ± 2500 V. The EMI-BF_4 emission current was relatively stable from ±1900 V to ±2300 V; whilst at higher voltages, the emission current experienced frequent sudden current surging and decaying. Electrospray current instability at high voltages has been observed in multiple studies [4, 6, 20], and it is believed that electrospray instability was induced by the over-stressed electric field applied at the emission sites on emitter tips. For EMI-BF_4 in these tests, the instability started to appear at ±500 V above its onset voltage, whilst the FAM-110A was still in a stable range when applied ±600 V above its onset voltage. However, the emission stability of FAM-110A at higher over-stressed voltages needs further investigation.

The FAM-110A thruster had an onset voltage was 400 V lower than the that of EMI-BF_4. The increasing rate of current over voltage between the two propellant are similar within the measured range. As a result, at the same voltage, the emission current using FAM-110A is higher than that of EMI-BF_4, meaning that FAM-110A would consume less power to generate the same level of emission current.

V. Secondary Species Emission

As illustrated in Figure 7(c), it was found that in both propellant IV plots, the positive current values were higher than the negative current values at the same voltage level, an effect more obvious at higher voltages. This discrepancy was likely due to the secondary species emission (SSE) from high-energy particles colliding with the collector plate, which altered the current signal received. In the tests shown in Figure 7, the SSE suppression grid was not applied with any voltage. A previous study has identified several possible SSE mechanisms associated with high-voltage electrospray devices testing in a vacuum facility, including secondary electron emission (SEE), sputtering or secondary ion emission, shock-induced desorption and splashing of droplets [21]. In order to identify the main SSE cause in these tests and

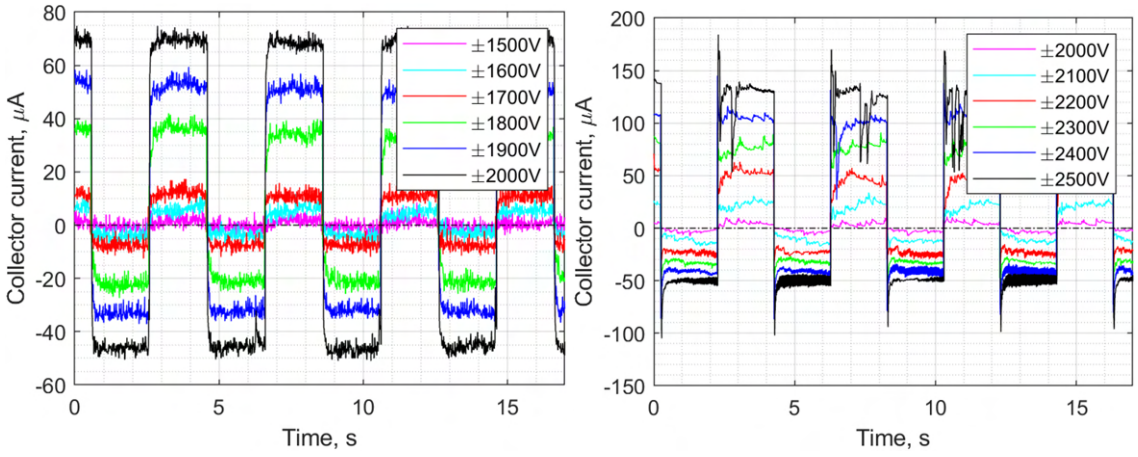

(a) Current stability plots of FAM-110A.

(b) Current stability plots of EMI-BF_4.

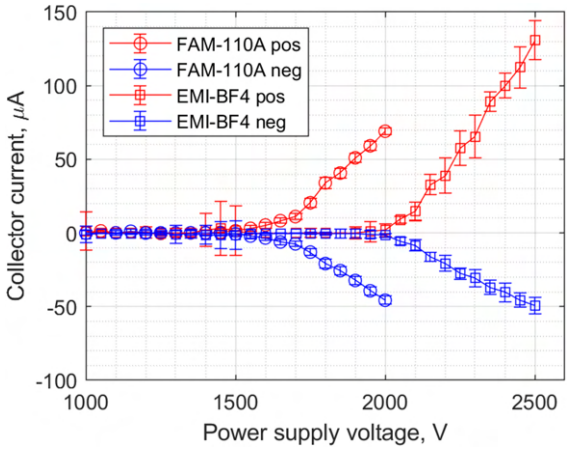

(c) IV plots of FAM-110A and EMI-BF_4. SSE suppression grid voltage was not applied.

Fig. 7 Current-voltage characteristics and current stability of electrospray thrusters using FAM-110A or EMI-BF_4 as propellant.

improve the accuracy of the collected current, the SSE grid in front of the collector plate was applied with a potential ranging from -100 V to 100 V, with the main collector plate kept at the ground potential. Using FAM-110A, the corresponding current-voltage characteristics with different SSE potentials are shown in Figure 8. These curves were plotted from raw collected data to show continuous current changes as the voltage increased. The vertical lines at different voltages represent the current variation range at the respective voltage.

In these SSE tests, the distance between the emitter tips and the upstream extractor surface was increased to approximately 0.5 mm to reduce the risk of short-circuiting. As a result, the onset voltages were higher than in the previous IV test, as shown in Figure 7. Accordingly, the maximum voltage applied between the emitter and extractor was increased to ±3000 V while the electrospray thruster was still in the regime of stable emission. The thruster was first tested with 0 V potential applied on the secondary species emission suppression grid (SSE grid), whose potential gradually decreased from -10 V to -100 V and then increased from +10 V to +100 V. Note that the emitter current level decreased progressively throughout the test campaign, in particular between the first two tests with SEE grid potential of 0 V and -10 V, as shown in Figure 8(c) and Figure 8(d).

With 0 V applied on the SSE grid, the positive collector current was higher than that of the negative part, agreeing with the previous tests as shown in Figure 7. With a negative potential applied to the SSE grid, as shown in Figure 8(a), the positive part of the current was significantly reduced, whilst the negative part only experienced slight changes. Even with a minor SEE grid potential of -10 V, at +3000 V, the current changed from +40 μA to +18 μA; whilst at -3000 V,

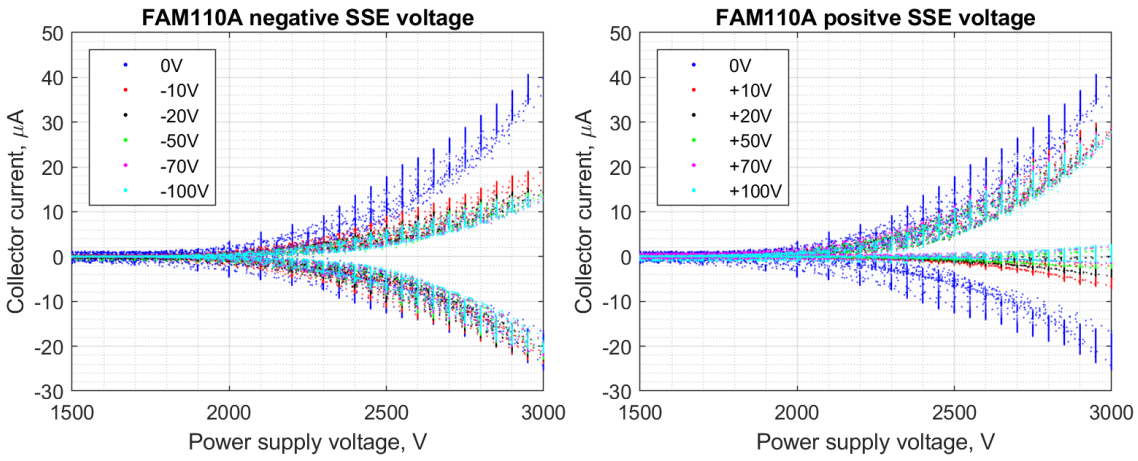

(a) Negative SSE voltages.

(b) Positive SSE voltages.

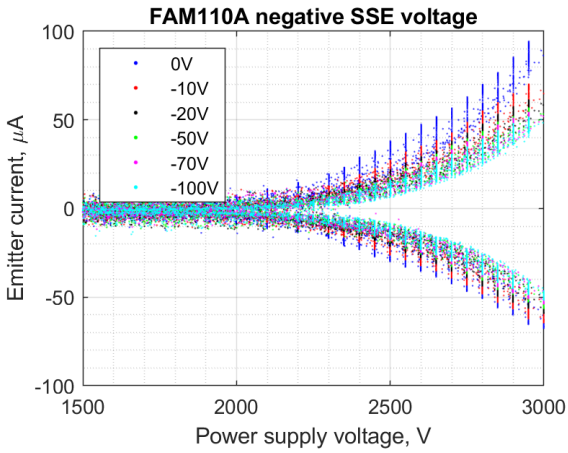

(c) Negative SSE voltages.

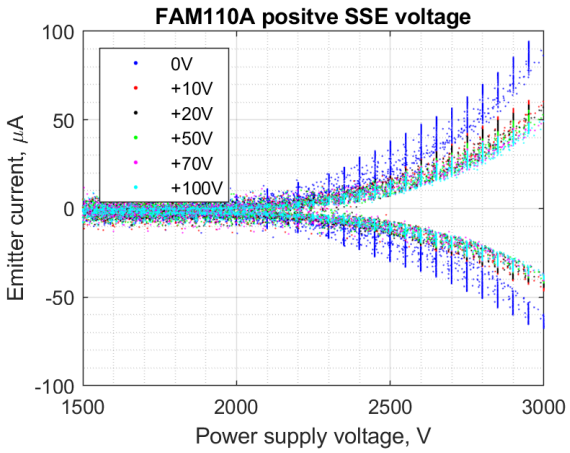

(d) Positive SSE voltages.

Fig. 8 Electrospray thruster collector current and emitter current I-V plots at different SSE suppression grid voltages.

the current amplitude was only reduced by 1 μ. At higher negative voltage on SSE grid voltage from -20 V to -100 V, the positive and negative collector current changes were small enough to be neglected. As shown in Figure 8(b), when the SSE grid is applied with a positive potential, U_{SSE}, the positive collector current experienced a slight decrease from 0 to +10 V of U_{SSE}, and remained the same values as U_{SSE} further increased up to +100 V. In comparison, the negative collector current showed significant changes. The negative current amplitude decreased drastically as U_{SSE} increased from 0 to +10 V, and continued changing toward positive values as U_{SSE} further increased. Interestingly, when U_{SSE} was between +50 V and +100 V, at negative thruster voltages, the collector should receive negative current readings, but instead it collected positive current signals.

Emission of secondary electrons and electrostatic sheath can explain most of these changes in collector current associated with different U_{SSE}. When high-energy particles collide on a metallic surface, there is a probability that the incoming particles will energize the metallic atoms and causes the emission of secondary particles, in particular, electrons. As the secondary electrons leave the collector plate, the plate would receive additional positive current signals. This process can happen at both the cation collisions and anion collisions. The molybdenum collector was connected to the ground through a 1 kΩ resistor. With the maximum collected current of $\pm$40 μA, the maximum potential of the collector plate was approximately $\pm$40 mV. As the collector plate is of near-ground potential, when the SSE grid is applied with a negative potential, the electric field between the SSE grid and the collector plate will suppress the electrons from backstreaming. The effectiveness of this electrostatic suppression depends on the voltage between the

collector plate and the SSE grid, and the energy of emitted secondary electrons. As the collisions between molybdenum and molecular ions are likely very complicated processes, it is reasonable to assume there is a distribution of energy of secondary electrons. In the SSE plots, an U_{SSE} of -10 V suppressed a significant portion of the emission, and -20 V effectively suppressed almost all the secondary electrons in both positive and negative emissions. It suggests that all the secondary electrons on the positive side had an energy of $\leqslant$20 eV, and within it, a majority had an energy of $\leqslant$10 eV. However, the negative side did not show such changes when U_{SSE} changed from 0 V to -100 V. A possible explanation is that the negatively charged emission particles created an electrostatic layer near the collector plate surface, which already suppressed the secondary electrons effectively, and thus, additional suppression voltages did not make a difference. In plasma applications, electrostatic sheath, also called Debye sheath, is a commonly found interaction between plasma and containment walls, [22, 23]. While in electrospray operation, the emission is generally of single-polarity and not quasi-neutral, so the electrostatic sheath is unlikely to form. However, the back-streaming secondary species from ions impingement on surfaces might change the charge state, possibly creating an electrostatic layer from a similar mechanism to an electrostatic sheath in plasma applications. This phenomenon is not yet well understood with electrospray sources. Nonetheless, this study provides insights into this problem, and further ion-wall interaction evidence can be found in Section VIII, where photos of significant light-emission near the collector plate surface were captured using long-exposure techniques.

The secondary electron emission and electrostatic layer also explain most of the collector current changes when U_{SSE} is positive, from 0 to +100 V. As the SSE grid is of higher potential to the collector plate, the electric field tends to enhance the emission of secondary electrons. This applied voltage could also affect the negatively-charged ions in the electrostatic layer, whose energies have been significantly reduced. As a result, the negative collector current gradually decreases in magnitude as U_{SSE} is increased. With U_{SSE} between +50 V and +100 V, the collector plate displayed positive current signals while receiving negatively-charged particles. This might be an indication that the secondary electron yield coefficient between some negatively-charged species and the molybdenum is higher than 1 at high voltages, meaning that one high-energy molecular ion's collision on the collector plate could 'knock out' one or more electrons from the plate. As a result, the positive current created by secondary electrons leaving the plate overpowers the negative current received from the negatively charged emission particles. It is also possible that the electrostatic layer created by these negatively charged particles still exits, but its spatial voltage that usually suppresses secondary electrons is gradually overpowered by the voltage between the SSE grid and the collector plate, causing releases of pre-suppressed electrons. When the collector plate receives positively-charged particles, the electrostatic layer would also be of higher potential, thus the emission of secondary electronss is not suppressed but enhanced. With U_{SSE} increased from +10 V to +100 V, the collector positive current kept almost the same values. The applied external electric field did not make a difference, possibly because all secondary electrons have already been emitted by the positive electrostatic layer.

However, the secondary electron emission and electrostatic layer cannot explain the positive collector current decreases with the U_{SSE} changed from 0 V to +10 V in Figure 8(b), where the amount of positive plume current read decreased markedly with a small increase in positive voltage to the SSE grid. In theory, these two curves should be the same, as is the case for data where U_{SSE} was between +10 V and +100 V. This difference may be caused by the emission of more complicated species in the plume, such as secondary ions, or fragmented particles upon collision with the grid or the plate. It may also be due to natural electrospray current decay as the device was tested for more than 30 mins between U_{SSE}=0 V test and the U_{SSE}=+10 V test.

It is unlikely that the emitted plume contained low-energy particles that caused these current changes. As discussed in Section VII, the same electrospray device was used in the retarding potential analysis study, and the results suggest that the majority of the plume particles have relatively high energy levels, closed to 100% of the emitter voltage.

This section provided some yet to be verified hypotheses to explain the current variations regarding different SSE grid potentials. Further investigations on this topic are encouraged. It would help researchers understand the interactions between high-energy molecular ions and surface materials and improve the experimental characterization systems for higher measurement accuracy.

VI. Spatial Plume Profile

This study investigated a method to profile the spatial distribution of electrospray thruster plume current. A motorized 2-axis rotary stage using stepper motors was designed, and it was remotely controllable using an Arduino microcontroller board. The stage can hold a thruster and rotate along two axes: a horizontal rotation (pitch axis) and a rotation along the thrust axis (roll axis). Both rotation axes were aligned with the center of the extractor, providing a higher positional accuracy in measurement. The plume current was measured using a Faraday cup, modified from

a retarding potential analyzer. The Faraday cup has an aperture of 10 mm, it has an SSE suppression grid placed in front of its collector, and the grid potential was set at -100 V. The Faraday cup was placed at a fixed position in the downstream of the plume. These rotations allow the plume measurement at any given angle, thus creating a complete two-dimensional plume profile. The plume profiling results of the FAM-110A are shown in Figure 9. In this case, the distance between the thruster and the Faraday cup was 30 cm. Each plot displays the horizontal plume profile of the thruster at different voltages, with a fixed angle along the roll axis. Four of these plots are shown here, with angles in the roll axis of -45, 0, 45, 90 degrees. The -45 and 45 degrees cases show the plume profiles along the two diagonal directions of the emitter tip array.

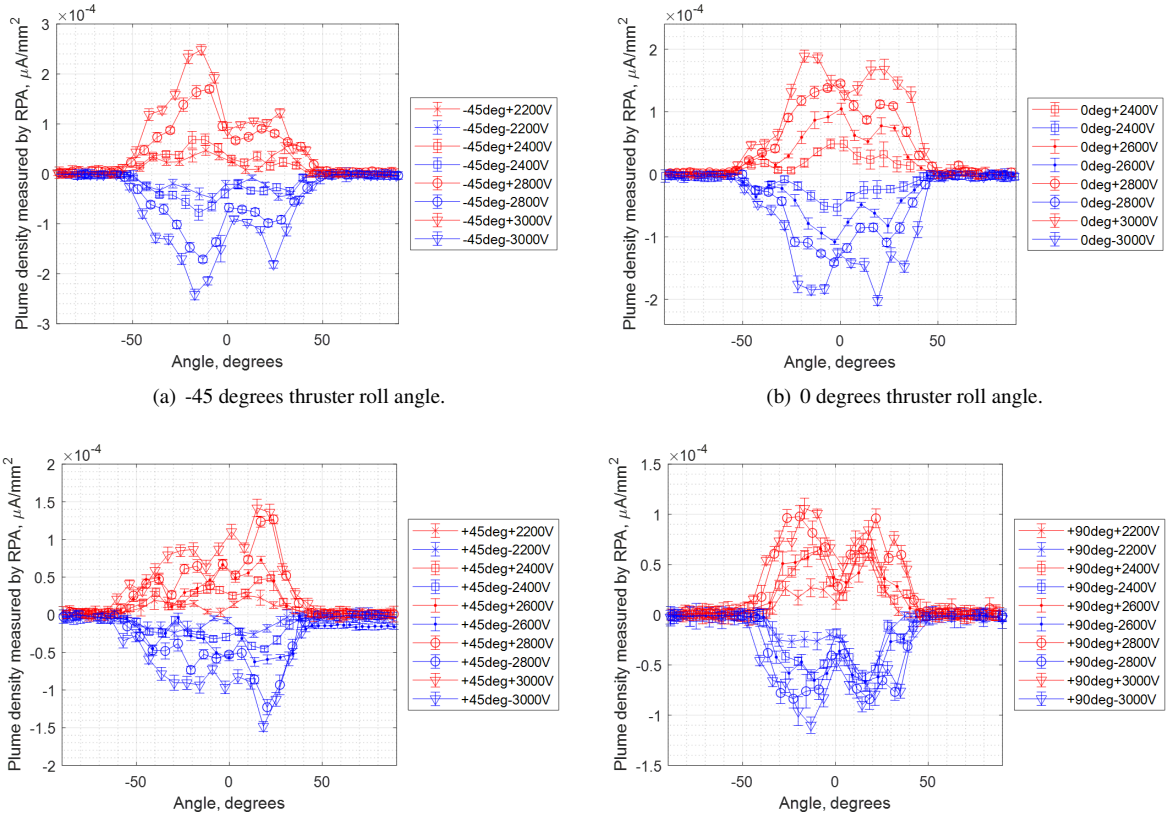

(a) -45 degrees thruster roll angle.

(b) 0 degrees thruster roll angle.

(c) +45 degrees thruster roll angle.

(d) +90 degrees thruster roll angle.

Fig. 9 Measured plume profiles at different thruster orientation angles (along the thrust axis) and at different thruster voltages using FAM-110A propellant.

It can be summarized that the plume profile was asymmetric along the roll axis. In order to explain this asymmetry, the extractor sheet was not rigid enough to be perfectly plain. Some apertures could be slightly closer to their respective emission tips, whilst others could be farther away during thruster assembly. The emitter in the plume profile study has already been tested for several hours in the IV study and SSE study before the plume profiling tests, meaning that the emission tips experienced different degrees of degradation. These geometric variations would lead to differences in onset voltage and emission current on each emission tip, resulting in asymmetrical plume profiles. The ideal approach for the plume profile study would be using a newly fabricated emitter chip along with a rigid extractor whose apertures align well with the emission tips. In this paper, being a primary subject of study, the emitter chip was the same in all tests, and as a result, degradation-induced emission inconsistency is unavoidable. The overall collected current density gradually decreased in value from tests at -45 degrees to tests at +90 degrees, another result of this electrospray thruster's inherent property of gradual emission current decay. Each plume profiling process took approximately 10 mins, and the thruster was tested for more than two hours before it was rotated along the roll axis to a different angle.

The plume current density increased with the applied voltage. There were two noticeable plume current density peaks in the cases of 0 degrees and +90 degrees, suggesting that across the 100 emitter tip array, there were at least

two specific emission sites outputting high emission current. In the case of 0 degrees, there was only one significant current density peak at low voltages, which gradually evolved into two peaks as the voltage increased, suggesting that the emission current increasing rates were different from these emission tips. The angular spread of plume current was wider at higher voltages, meaning that the plume angle increased with the applied voltage. Defining the plume angle as the angular spread containing 95% of the total emission current, the thruster using FAM-110A at ±3000 V had a plume half-angle of approximately 48 degrees.

The plume profile of the thruster using EMI-BF_4 was measured using a similar method, and the results at 0 degrees in the roll axis are shown in Figure 10. The plume profile is also converted to a two-dimensional spatial distribution in Figure 10(b) to provide a more intuitive demonstration. The positive currents are plotted upwards, the negative currents are plotted downwards, the length of each represents the current intensity, and the angle of each line represents its pointing angle in 1:1 aspect ratio two-dimensional space. Similar to the thruster using FAM-110A, the measured plume current density increased with the applied voltage, and the plume angle also increased with applied voltage, which is approximately 62 degrees in half-angle. In these two plume profiling tests, FAM-110A thruster demonstrated a slightly smaller plume half-angle, thus higher angular efficiency. The symmetricity of EMI-BF_4 was slightly better, though two noticeable current peaks were still noticeable. However, the symmetricity and plume angle comparison between the EMI-BF_4 thruster and the FAM-110A thruster are not conclusive because they depend on several geometrical variables, including the alignment between the emitter and the extractor, and thus, might vary slightly between each test.

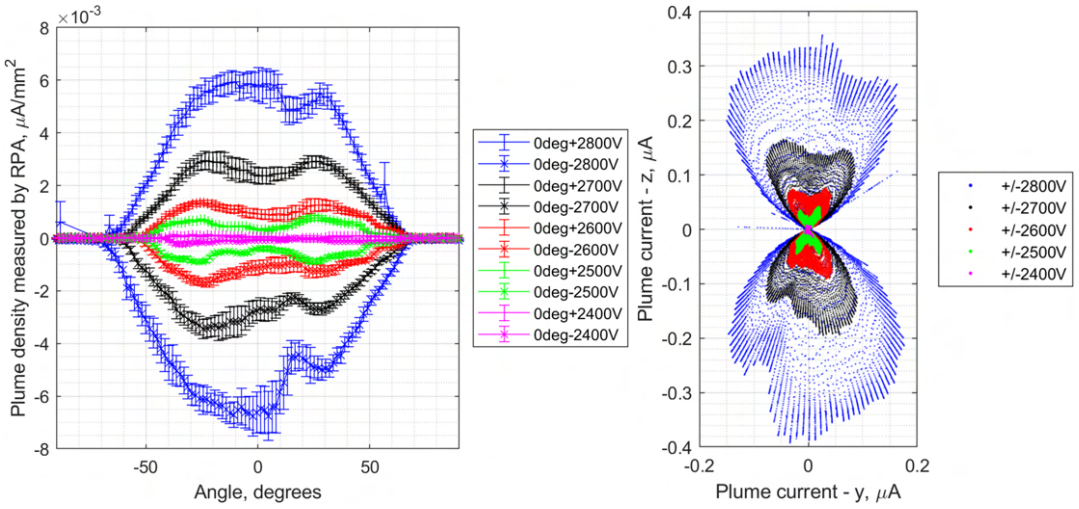

(a) 0 degrees thruster rotation angle.

(b) Spatial distribution of the plume profile.

Fig. 10 Measured plume profiles at different thruster voltages using EMI-BF_4 propellant.

VII. Particle Energy Analysis

A retarding potential analyzer was designed and used to measure the energy distribution of emitted particles, with the RPA used being an upgraded version of a previous RPA design [17]. The RPA consisted of 5 electrodes, which were a grounded shield and a grid, a secondary species emission (SSE) suppression grid (set to -100 V potential), HV retarding potential grid (HVRP grid), a second SSE suppression grid and a stainless steel collector plate. The RPA collector surface was designed with concentric 20 degrees sharp zigzag structures, which act as chevron configurations to reduce the SSE from impinging particles, giving more accurate current measurements. In RPA tests, the HVRP grid was applied with a sweeping high voltage, allowing charged particles of different kinetic energies to be stopped from colliding on the collector, whose signals can be used to characterize the energy distribution of the plume particles, the non-kinetic efficiency and the effects of fragmentation. The RPA results of the FAM-110A thruster are shown in Figure 11.

The axes are normalized, and the results at different voltages in their respective polarity are relatively consistent, especially at negative voltages. In both polarities, there is a major RPA signal step near the normalized retarding potential of 1, suggesting that the effective acceleration voltage is almost the same as the power supply voltage with only about

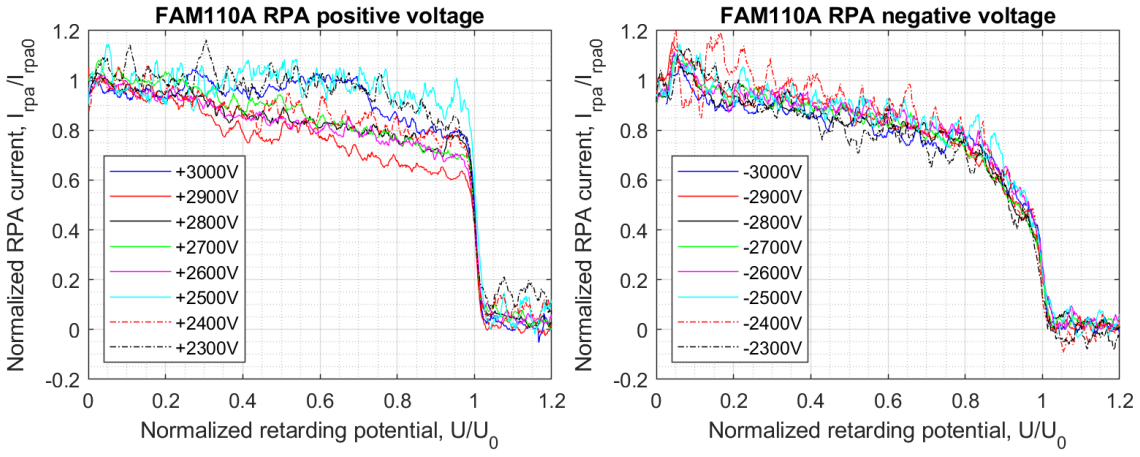

(a) Positive thruster voltages.

(b) Negative thruster voltages.

Fig. 11 Retarding potential analysis results of the electrospray thruster running using FAM-110A propellant at different thruster voltages.

2% of voltage losses, resulting in the non-kinetic efficiency being approximately 98%. The downward-sloping lines or curves that exist in all RPA traces are evidence of fragmentation of the emitted particles. Similar features were found in a previous RPA study using EMI-BF_4, in which two significant current steps were usually found at different voltages, along with similar downward sloping lines or curves between the current steps [17]. These downward lines covering the entire range of retarding potential axis suggest that a portion of the particles did not fully utilize the acceleration energy, possibly with fragmentation occurring within the acceleration electric field. FAM-110A thruster RPA data did not show a second noticeable current step like those with EMI-BF_4 data, suggesting that particles did not fragment in the field-free region between the extractor and the RPA collector. Noticeably, in RPA data at the negative voltages, there are segments with sudden slope changes in the U/U_0 range from 0.85 to 0.98. This could be fragmentation occurring rather close to the emission tips, where the electric field is more substantial. This is because if a particle fragments earlier in the acceleration field, the loss of energy from the fragmented neutral particle will be less, so the retained energy of the charged particle after fragmentation will be closer to 1.

From these RPA results, it can be summarized that the emitter plume of FAM-110A propellant is more mono-energetic than that of EMI-BF_4, which is beneficial to efficiency as the energy loss caused by neutral particles from fragmentation would be less. There is still fragmentation evidence of emitted FAM-110A particles, especially at the negative polarities, which only occur in a strong electric field near the emission tips. This can be further investigated with simulation tools to estimate the critical electric field strength that would cause such fragmentation, providing thruster design suggestions.

VIII. Light Emission in Electrospray

Electrospray thrusters were long thought not to show any glow when tested in a vacuum. However, light emission was observed in multiple recent electrospray studies [21, 24–26], including a previous development of the PET-100 thruster [27]. A recent study from the University of California, Los Angeles, investigated the relationship between thruster glowing and vacuum facility effects, coming to the conclusion that the emission of secondary species is a primary cause for the light emission in electrospray thrusters [21, 24]. Here we investigated the light emission phenomenon with PET-100 electrospray thrusters using different ionic liquid propellants based on the recommended long-exposure photography techniques.

Both FAM-110A and EMI-BF_4 propellants were tested. A Nikon D5300 DSLR camera was used to capture the photos of light emissions. It was quickly found out that there were two primary regions where the glowing appeared: the region near the electrospray thruster extractor and the region near the particle impingement location on a downstream plate. Example photos of different propellants and different impingement plate materials (aluminum and 316 stainless steel) are shown in Figure 12. The camera settings for these images were: exposure time 30 s, ISO 12800, and focus F5.6. No additional filters were used.

Due to the light emitted from a sub-milliampere electrospray source was inherently dim, the long-exposure turned

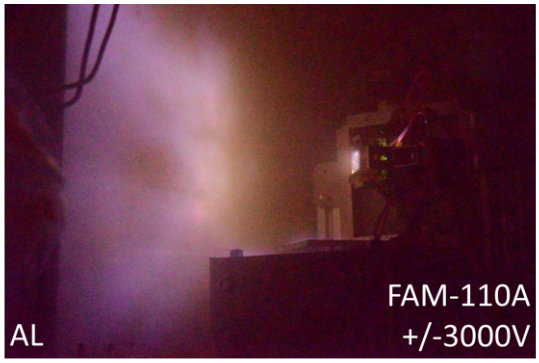

(a) Aluminum plate using FAM-110A, with the thruster pitch angle of -45 degrees.

(b) Porous 316 stainless steel plate using FAM-110A, with the thruster pitch angle of 0 degrees.

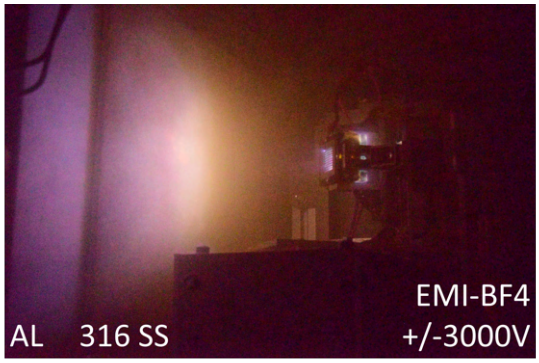

(c) Aluminum plate using EMI-BF_4, with the thruster pitch angle of -45 degrees.

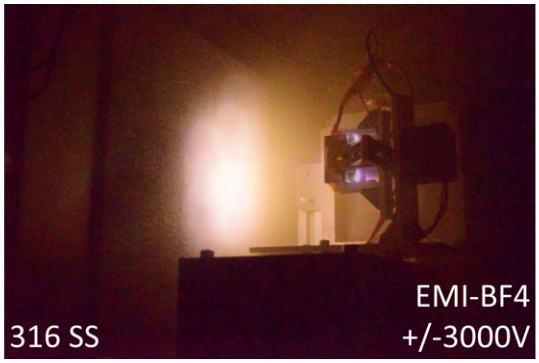

(d) Porous 316 stainless steel plate using EMI-BF_4, with the thruster pitch angle of 0 degrees.

Fig. 12 Light emission from different impinging plate materials using different ionic liquid propellants.

out to be an effective method for studying this phenomenon. The glowing pattern on the collector indicates the two-dimensional profile of the intercepted plume, and the brightness is an indication of the emission current density and energy of the impinging particles. The size and brightness of the glowing pattern increased with the thruster voltage. This offers a new way to characterize the 2D plume profile of an electrospray device instantaneously. From the photos, it can be found that the glowing pattern of the FAM-110A thruster was more irregular compared to that of the EMI-BF_4 thruster, which explains the non-uniformity of the plume profiling results as discussed in Section VI.

The colors of the glow were quite similar between the two ionic liquid propellants tested; however, the glow on the aluminum plate was near purple, whilst the glow on the 316 stainless steel plate was more in the yellow/orange spectrum.

The sources behind the light emission are still not clear at the current stage. There are three hypotheses: the light may be emitted from excited metallic atoms created by sputtering, ionized propellant molecules emitted from the thruster, or excited propellant molecules energized by secondary electrons. The color of the glow may suggest what the sources of the glow are, and an optical emission spectroscopy test is currently being conducted to measure the spectrum. A systematic investigation has been conducted to study the glow variations at different test conditions. This glow study should also offer insights into the near-wall electrostatic layer created by impinging charged particles. The glow near the thruster may be due to the interaction between emitted particles and the extractor material, with backstreaming particles from the downstream plate. This will likely affect the thruster lifetime and emission stability, thus, further investigations are required.

IX. Conclusion

The FAM-110A propellant designed for electrospray-decomposition dual-mode propulsion systems was studied in this paper. The propellant was synthesized and, for the first time, tested in a PET-100 electrospray thruster with a porous

emitter. The thruster operated successfully and demonstrated stable emission currents. Compared to the benchmark EMI-BF_4 propellant, the FAM-110A thruster had lower onset voltages and relatively high emission current. A range of plume properties of the FAM-110A thruster were investigated. It was found that secondary species emissions play an influential role in measuring emitted current, which can be corrected by applying a suppression electric field. With a rotary stage, the plume profile was measured and appeared to be asymmetric after several tests, though this could be improved significantly with better emitter-extractor alignment. The plume half-angle of the FAM-110A thruster was about 48 degrees, which is smaller than 62 degrees of the EMI-BF_4 thruster. The energy of the FAM-110A plume particles was characterized, which appeared to be more mono-energetic than EMI-BF_4, resulting in higher efficiency. Light emission was observed in both the FAM-110A thruster and the EMI-BF_4 thruster, near the thruster and the downstream impinging plate. A range of investigations is in progress to understand this phenomenon and mitigate its effects on thruster lifetime, emission stability and measurement accuracy.

This study provided valuable information on plume properties and efficiency from operating an electrospray thruster with a porous emitter that uses the novel ionic liquid propellant FAM-110A. The FAM-110A ionic liquid propellant demonstrated promising performance in an electrospray thruster with a porous emitter. Further studies of FAM-110A-based electrospray sources are recommended.

X. Acknowledgment

The research reported here was partially supported by the Defense Advanced Research Projects Agency Grant No.: HR00112110003. The content of this paper does not necessarily reflect the position or the policy of the Government, and no official endorsement should be inferred. We want to thank the Engineering Design and Manufacturing Centre (EDMC) at the University of Southampton for manufacturing our testing equipment.

XI. Data Availability

The data that support the findings of this study are available from the corresponding author upon reasonable request.

References

[1] Krejci, D., and Lozano, P., "Space Propulsion Technology for Small Spacecraft," *Proceedings of the IEEE*, Vol. 106, No. 3, 2018, pp. 362–378.

[2] Courtney, D. G., Dandavino, S., and Shea, H., "Performance and Applications of Ionic Electrospray Micro-Propulsion Prototypes," *AIAA Space 2015*, 2015, pp. 1–10.

[3] Hudson, J., Spangelo, S., Hine, A., Kolosa, D., and Lemmer, K., "Mission Analysis for CubeSats with Micropropulsion," *Journal of Spacecraft and Rockets*, 2016, pp. 0–0.

[4] Natisin, M. R., Zamora, H. L., Holley, Z. A., Ivan Arnold, N., McGehee, W. A., Holmes, M. R., and Eckhardt, D., "Efficiency Mechanisms in Porous-Media Electrospray Thrusters," *Journal of Propulsion and Power*, Vol. 37, No. 5, 2021, pp. 650–659.

[5] Lemmer, K., "Propulsion for CubeSats," *Acta Astronautica*, Vol. 134, No. February, 2017, pp. 231–243.

[6] Ma, C., Bull, T., and Ryan, C. N., "Plume Composition Measurements of a High-Emission-Density Electrospray Thruster," *Journal of Propulsion and Power*, Vol. 37, No. 6, 2021, pp. 816–831.

[7] Rovey, J. L., Lyne, C. T., Mundahl, A. J., Rasmont, N., Glascock, M. S., Wainwright, M. J., and Berg, S. P., "Review of multimode space propulsion," *Progress in Aerospace Sciences*, Vol. 118, 2020, p. 100627.

[8] Berg, S. P., Rovey, J., Prince, B., Miller, S., and Bemish, R., "Electrospray of an Energetic Ionic Liquid Monopropellant for Multi-Mode Micropropulsion Applications," *51st AIAA/SAE/ASEE Joint Propulsion Conference*, AIAA Propulsion and Energy Forum, American Institute of Aeronautics and Astronautics, 2015.

[9] Mundahl, A. J., Berg, S. P., Rovey, J., Huang, M., Woelk, K., Wagle, D., and Baker, G., "Characterization of a Novel Ionic Liquid Monopropellant for Multi-Mode Propulsion," *53rd AIAA/SAE/ASEE Joint Propulsion Conference*, AIAA Propulsion and Energy Forum, American Institute of Aeronautics and Astronautics, 2017.

[10] Lyne, C. T., Rovey, J., and Berg, S. P., "Monopropellant-Electrospray Multimode Thruster Testing Results: Electrospray Mode," *AIAA Propulsion and Energy 2021 Forum*, AIAA Propulsion and Energy Forum, American Institute of Aeronautics and Astronautics, 2021.

[11] Eisen, J., Cline, B., Berg, S. P., and Rovey, J., "Power Processing Unit and Feed System Development for a Multimode Spacecraft Propulsion System," *AIAA Propulsion and Energy 2021 Forum*, AIAA Propulsion and Energy Forum, American Institute of Aeronautics and Astronautics, 2021.

[12] Falcone, G., Engel, D., Ryan, C. N., Rovey, J. L., Putnam, Z. R., Berg, S. P., and Lembeck, M., "Mission Performance Assessment of Multimode Propulsion for Satellite Servicing Applications," *IEEE Aerospace Conference*, Big Sky, MT., 2022.

[13] Sharma, A., Adducci, A. C., Rovey, J., Ma, C., Ryan, C. N., Berg, S., Lembeck, M., and Putnam, Z. R., "Green Ionic Liquid Multimode Monopropellant Based Chemical Micro-thruster," *AIAA SCITECH 2022 Forum*, AIAA SciTech Forum, American Institute of Aeronautics and Astronautics, 2021.

[14] Freudenmann, D., and Ciezki, H. K., "ADN and HAN-Based Monopropellants – A Minireview on Compatibility and Chemical Stability in Aqueous Media," *Propellants, Explosives, Pyrotechnics*, 2019, pp. 1084–1089.

[15] Azuma, N., Hori, K., Katsumi, T., and Amrousse, R., "Research and Development on Thrusters with HAN (Hydroxyl Ammonium Nitrate) Based Monopropellant," *5th European Conference for Aerospace Sciences (EUCASS)*, Vol. 163, No. 1, 2013, pp. 5–10.

[16] Reed, B., and Harasim, S., "Material compatibility testing with HAN-based monopropellants," *37th Joint Propulsion Conference and Exhibit*, Joint Propulsion Conferences, American Institute of Aeronautics and Astronautics, 2001.

[17] Ma, C., and Ryan, C., "Plume Particle Energy Analysis of an Ionic Liquid Electrospray Ion Source with High Emission Density," *Journal of Applied Physics*, Vol. 129, No. 083302, 2021, pp. 1–11.

[18] Ma, C., Messina, V., Ryan, C. N., Rovey, J. L., Putnam, Z. R., Lembeck, M., and Berg, S., "Emission Characterization of Porous Electrospray Thrusters with Actively Controlled Flow Rate," *Proceedings of the 37th International Electric Propulsion Conference*, Electric Rocket Propulsion Society, Cambridge, MA, 2022.

[19] Ma, C., "Design and Characterisation of Electrospray Thrusters with High Emission Density," Ph.D. thesis, University of Southampton, 2020.

[20] Krejci, D., Mier-Hicks, F., Thomas, R., Haag, T., and Lozano, P., "Emission Characteristics of Passively Fed Electrospray Microthrusters with Propellant Reservoirs," *Journal of Spacecraft and Rockets*, Vol. 54, No. 2, 2017, pp. 447–458.

[21] Uchizono, N. M., Collins, A. L., Marrese-Reading, C., Arestie, S. M., Ziemer, J. K., and Wirz, R. E., "The role of secondary species emission in vacuum facility effects for electrospray thrusters," *Journal of Applied Physics*, Vol. 130, No. 14, 2021.

[22] Breizman, B. N., and Kiramov, D. I., "Plasma sheath and presheath development near a partially reflective surface," *Journal of Plasma Physics*, Vol. 87, No. 1, 2021.

[23] Vanraes, P., and Bogaerts, A., "The essential role of the plasma sheath in plasma-liquid interaction and its applications—A perspective," *Journal of Applied Physics*, Vol. 129, No. 22, 2021.

[24] Uchizono, N. M., and Wirz, R. E., "Facility Effects for Electrospray Thrusters," *AIAA SCITECH 2022 Forum*, AIAA SciTech Forum, American Institute of Aeronautics and Astronautics, 2021.

[25] Chen, C., Chen, M., Fan, W., and Zhou, H., "Effects of non-uniform operation of emission sites on characteristics of a porous electrospray thruster," *Acta Astronautica*, Vol. 178, No. September 2020, 2021, pp. 192–202.

[26] Máximo, D. V. M., and Velásquez-García, L. F., "Additively manufactured electrohydrodynamic ionic liquid pure-ion sources for nanosatellite propulsion," *Additive Manufacturing*, Vol. 36, 2020.

[27] Ma, C., and Ryan, C. N., "Characterization of a Micro-electrospray Thruster with a Porous Glass Emitter Array," *Proceedings of the Space Propulsion Conference 2018*, 2018, pp. 1–12.